Deep Learning Guided Diffusion MRI Tractography in the Mouse Brain

Zifei Liang[1], Tanzil Mahmud Arefin[1], Choong H. Lee[1], Jiangyang Zhang[1]

[1] Bernard and Irene Schwartz Center for Biomedical Imaging, Department of Radiology, New York University School of Medicine, New York, NY 10016, USA

Corresponding to:

Jiangyang Zhang, Ph.D.
Center for Biomedical Imaging,
Department of Radiology,
New York University School of Medicine,
660 First Ave.
New York, NY 10016, USA
Jiangyang.zhang@nyulangone.org

Abstract

Diffusion MRI (dMRI) tractography is the only tool for non-invasive mapping of macroscopic structural connectivity of the entire brain. Although it has been successfully used to reconstruct large white matter tracts in the human and animal brains, the sensitivity and specificity of dMRI tractography, remained limited. Especially, the fiber orientation distributions (FODs) estimated from dMRI signals, which is key to tractography, may deviate from histologically measured fiber orientation in crossing fibers and gray matter regions. In this study, we demonstrated that a deep learning network, trained using mesoscopic tract-tracing data from the Allen Mouse Brain Connectivity Atlas, was able to improve the estimation of fiber orientations from mouse brain dMRI data. Tractography results based on the network-generated fiber orientations showed improved specificity while maintaining sensitivity comparable to conventional dMRI tractography. Our result is a proof-of-concept of how mesoscale tract-tracing data can guide dMRI tractography and enhance our ability to characterize brain connectivity.

Keywords: Diffusion MRI, tractography, mouse brain, deep learning, fiber orientation distribution, connectivity

Introduction

The introduction of diffusion MRI (dMRI) based tractography about 20 years ago generated great excitement due to its promise of tracing white matter tracts in the brain non-invasively (Mori and van Zijl 2002; Jbabdi et al. 2015; Basser and Jones 2002). Aided by increasingly sophisticated dMRI acquisition schemes and tractography methods (Frank 2001; Tuch et al. 2002; Wedeen et al. 2012; Wedeen et al. 2008; Behrens et al. 2007; Mori and van Zijl 2002; Tournier, Calamante, and Connelly 2007), dMRI tractography had gained the ability to resolve multiple axonal bundles within a voxel as well as higher sensitivity to small white matter tracts than the original diffusion tensor imaging-based tractography. To this date, dMRI tractography remains the only tool for non-invasive mapping of macroscopic structural connectivity of the entire brain.

Current routine dMRI tractography starts with the estimation of the fiber orientation distribution (FOD) in each voxel from dMRI signals (Tournier, Calamante, and Connelly 2007), followed by the generation of streamlines connecting neighboring voxels based on FODs using deterministic or probabilistic algorithms (Behrens et al. 2007; Mori and van Zijl 2002). While numerous studies in human and animal brains have demonstrated the capabilities of dMRI tractography in visualizing tract trajectories and estimating structural connectivity between brain regions under normal and pathological conditions, e.g. (Lo et al. 2010; White et al. 2020; Jbabdi et al. 2015; Catani et al. 2002), its limitations have also been recognized (Jbabdi and Johansen-Berg 2011; Jones, Knosche, and Turner 2013), and efforts have been made to understand the underlying causes in order to circumvent or alleviate these limitations.

The limitations of dMRI tractography has been explored by numerous studies that compared tractography results with chemical and viral tracer findings from post-mortem brain specimens, e.g. (Seehaus et al. 2013; Aydogan et al. 2018; Calabrese et al. 2015; Chen et al. 2015; Azadbakht et al. 2015; Grisot, Haber, and Yendiki 2021; Dyrby et al. 2007; Howard et al. 2019). While these studies demonstrated good agreements for major white matter tracts, they also revealed noticeable differences when tractography results entered superficial white matter and gray matter regions (Thomas et al. 2014;

Reveley et al. 2015; Wu and Zhang 2016; Maier-Hein et al. 2017; Schilling et al. 2019; Grisot, Haber, and Yendiki 2021; Howard et al. 2019). Several ways to improve dMRI tractography have been explored, such as improving spatial resolution (Poot et al. 2013; Calabrese et al. 2014; Liebrand et al. 2020) and optimizing tractography parameters (Gutierrez et al. 2020; Schurr et al. 2018; Fillard et al. 2011; Moldrich et al. 2010), but the primary focus has been on comparing FODs estimated from dMRI signals and axon orientation distributions measured using optical techniques, for instance, confocal microscopy (Schilling et al. 2016; Schilling et al. 2018) , polarized light imaging (Mollink et al. 2017), and optical coherence tomography (Jones et al. 2020). These studies generally demonstrated good but not perfect agreements between estimated FODs and axonal pathways, highlighting the challenges of inferring tissue axonal organization from dMRI signals.

In this study, we investigated whether deep learning could improve the estimation of fiber orientations from dMRI signals. While several widely used estimators of FODs are based on tissue diffusion models for myelinated axons (Tournier, Calamante, and Connelly 2007), tissue microstructure in gray matter is more complex than the white matter with additional cellular compartments, and our knowledge of how to model dMRI signals from gray matter remains limited. In comparison, the deep learning framework is data-driven and model-free, and there have been several reports on using machine and deep learning to predict MRI-based tissue parameters, including FODs, from MRI signals (Lin et al. 2019; Gibbons et al. 2019; Li et al. 2021). Our recent study has demonstrated that the deep learning framework can be used to generate virtual histology from MRI signals by training a network with co-registered MRI and histological data (Liang et al. 2022). The data from the Allen Mouse Brain Connectivity Atlas (AMBCA)(Oh et al. 2014; Kuan et al. 2015; Lein et al. 2007), which contains an immense database of viral tracer data of the mouse brain captured using serial two-photon microscopy, provide rich information on mouse brain structural connectivity at the mesoscopic level. Based on streamlines reconstructed from individual data in AMBCA following tracer propagation, we constructed a mouse brain streamline dataset, based on which maps of track orientation distribution (TOD) (Dhollander et al. 2014)

were generated. The 3D TOD dataset was then co-registered with ex vivo mouse brain dMRI data and used to train a network to predict voxel-wise TODs from dMRI signals.

2. Methods

2.1. Generation of a symmetric whole brain streamline dataset from AMBCA

The AMBCA provides tracer streamlines that represent axonal trajectories in each tracer experiment generated using a fast-marching algorithm (Fig. 1A-B). The tracer streamlines from 2,764 independent experiments were downloaded from AMBCA (http://api.brain-map.org/examples/lines/index.html) and converted from the original JSON format into the TCK format used by MRtrix (www.mrtrix.org)(Tournier et al. 2019). As all the tracer data have been normalized to the Allen Reference Atlas (ARA) space, the streamlines from all experiments were summed to form a large streamline dataset (Fig. 1C). As most injection sites in AMBCA experiments were located in one hemisphere, uneven streamline densities between the two hemispheres were observed (Fig. 1C). To resolve this issue, all streamlines were flipped left-right along the midline of the brain, and the flipped streamlines were added to the original streamlines to form a symmetric whole brain streamline dataset (Fig. 1D), which contained 3,765,678 (~ 4 million) streamlines. We called this dataset and the streamlines in it the AMBCA streamline dataset and AMBCA streamlines, respectively.

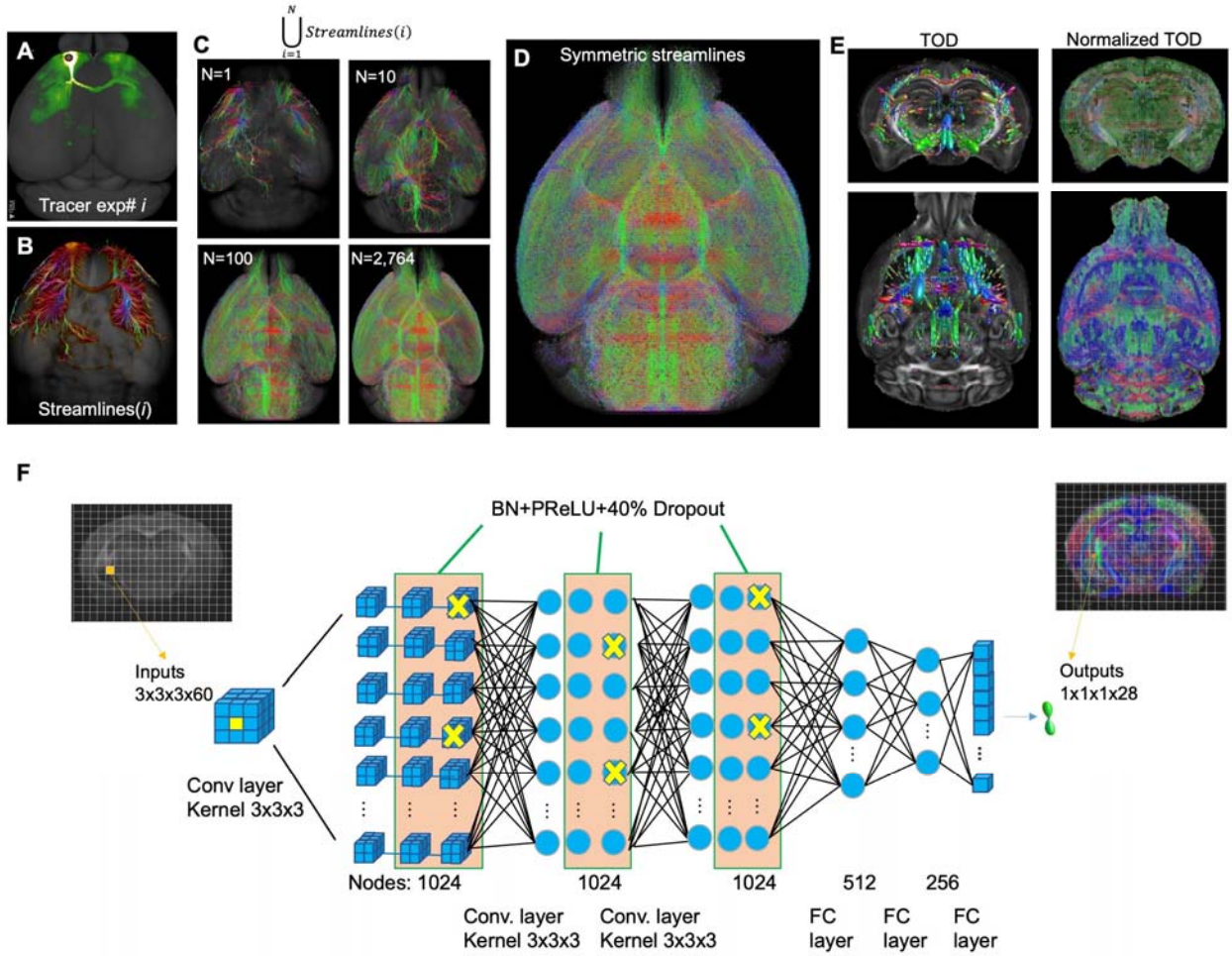

Fig. 1: *Generation of symmetric whole-brain tracer streamlines from AMBCA and training a deep neural network to predict fiber orientation.* ***A-B:*** *A representative tracer experiment (ID# 100140756) and its corresponding streamlines generated using a fast-marching algorithm.* ***C:*** *The process of collecting streamlines from all 2,764 injection experiments, with injection sites mainly located in one hemisphere.* ***D:*** *A symmetric 4-million streamline dataset was generated by flipping the streamlines in* ***C*** *along the midline and added to the original streamline dataset.* ***E:*** *Track orientation density (TOD) maps based on the AMBCA streamlines and normalized TOD maps.* ***F:*** *The basic architecture of TODNet. The inputs to the network are 3x3x3 voxel patches, with a N-vector signals in each voxel, and the outputs are normalized TODs with 28 spherical harmonic coefficients. The network basic setting is 1024-1024-1024-512-256, each number represents the output neurons in each layer. In the first three 1024-1024-1024 layers, 40% neurons were dropped-off for regularization.*

2.2. Generation of streamline dataset from cell tracing data

The single-cell dataset in the MouseLight project was downloaded from its website (http://ml-neuronbrowser.janelia.org/) (Winnubst et al. 2019), which contained reconstruction for more than 1,000 long-range projection neurons with axons traveling over long distances and across multiple brain regions. The downloaded axon tracing data were converted from the original JSON format into the TCK format used by MRtrix (www.mrtrix.org). As all the single-cell data have been normalized to the ARA space, the streamlines from many cells could be combined into one dataset similar to what we did for the AMBCA streamline dataset.

2.3. Ex vivo mouse brain diffusion MRI

All animal experiments have been approved by the Institute Animal Care and Use Committee at New York University. Adult C57BL/6 mice (P56, n=10, Charles River, Wilmington, MA, USA) were perfusion fixed with 4% paraformaldehyde (PFA) in PBS. The samples were preserved in 4% PFA for 24 hours before transferring to PBS. *Ex vivo* MRI of mouse brain specimens was performed on a horizontal 7 Tesla MR scanner (Bruker Biospin, Billerica, MA, USA) with a triple-axis gradient system. Images were acquired using a quadrature volume excitation coil (72 mm inner diameter) and a receive-only 4-channel phased array cryogenic coil. The specimens were imaged with the skull intact and placed in a syringe filled with Fomblin (perfluorinated polyether, Solvay Specialty Polymers USA, LLC, Alpharetta, GA, USA) to prevent tissue dehydration (Arefin et al. 2021). Three-dimensional diffusion MRI data were acquired using a modified 3D diffusion-weighted gradient- and spin-echo (DW-GRASE) sequence (Aggarwal et al. 2010; Wu et al. 2013) with the following parameters: echo time (TE)/repetition time (TR) = 30/400ms; two signal averages; field of view (FOV) = 12.8 mm x 10 mm x 18 mm, resolution = 0.1 mm x 0.1 mm x 0.1 mm; two non-diffusion weighted images (b_0s); 60 diffusion weighted images (DWIs) with a diffusion weighting (b) of 5,000 s/mm^2.

From the dMRI data, diffusion tensors were calculated using the log-linear fitting method implemented in MRtrix (http://www.mrtrix.org) at each pixel, and maps of mean

and radial diffusivities and fractional anisotropy were generated. FOD maps were generated using spherical deconvolution using MRtrix as described in (Arefin et al. 2021). Mappings between individual MRI data and the ARA space were computed using the Large Deformation Diffeomorphic Metric Mapping (LDDMM) method (Ceritoglu et al. 2009) implemented in the DiffeoMap software (www.mristudio.org) as described in(Lim et al. 2013; Ceritoglu et al. 2009). These mappings were diffeomorphic (one-to-one and differentiable) and allowed us to transform the symmetric whole-brain streamline data from AMBCA to individual subject space without changing the topology of the streamline network.

2.4. Estimation of tract-orientation-distribution (TOD) from the streamline dataset.

The AMBCA streamlines were mapped from the ARA space to each subject using the mappings generated using LDDMM. A 3D TOD map was then generated from the streamline data mapped into the subject space using the tckmap command in MRtrix with the maximum spherical harmonic degree (lmax) set to 6 (Dhollander et al. 2014). The orientation and amplitude of the TOD reflected the number and arrangement of AMBCA streamlines at each voxel after mapping. Using the initial TODs, we computed short streamlines with lengths less than 6 mm and then generated the so-called level 2 TODs based on the short streamlines, as described in (Dhollander et al. 2014). As the amplitudes of TODs generated from the AMBCA streamline data depend on the distribution of injection sites and may not reflect the actual number of axons, the amplitudes of TODs were normalized so that the maximum TOD coefficient at each voxel was set to 1. We called the normalized TODs and 3D TOD map the AMBCA TODs and AMBCA TOD maps, respectively.

2.5. Deep learning neural network to predict TODs from dMRI signals

We started with a network described in (Lin et al. 2019), which can be trained to predict FODs from dMRI signals. The network consisted of two convolution layers and four fully connected layers. The inputs to the network were patches that contained 3x3x3 voxels from the dMRI data of each subject (2 non-diffusion-weighted and 60 diffusion-weighted), and the outputs of the network were 28 FOD coefficients. The

network was implemented in Python using Keras (www.github.com/fchollet/keras), and the training was performed on a desktop GPU (NVIDIA RTX 2080). MRI data from 10 subjects were randomly assigned to training (n=6) and testing (n=4) groups. One million 3x3x3 patches from the training mouse brain dMRI data and their corresponding FODs were used for training, within which 10% was used as the validation cohort. Using the testing data as inputs to the trained network, the predicted FODs agreed well with FODs estimated from the same data using MRtrix (Supplementary Figure 1).

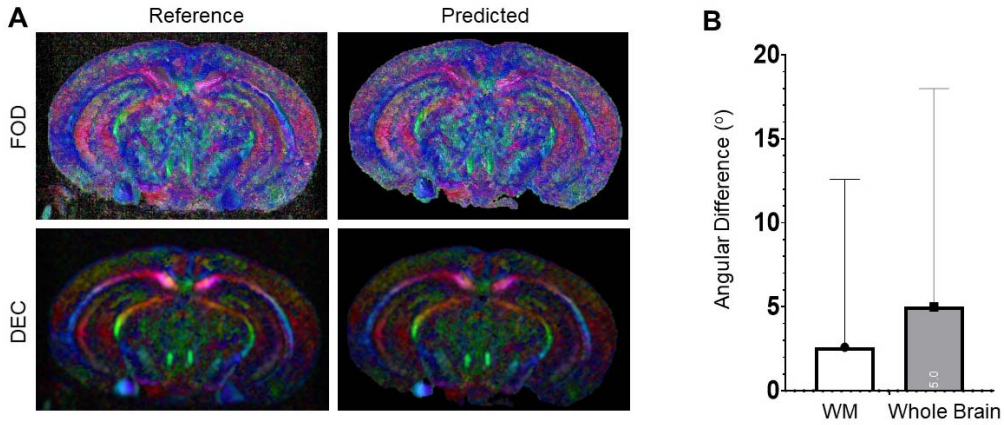

Supplementary Fig. 1: *A comparison of predicted FODs and FODs from spherical deconvolution in the mouse brain.* ***A:*** *The FOD map and directionally encoded colormap generated using the network introduced by Lin et al. (Lin et al. 2019) and trained using ex vivo mouse brain dMRI data (predicted) showed good agreements with results generated using MRtrix (Reference).* ***B:*** *The differences in primary orientation of predicted and reference FODs were* $3^o \pm 10.0^o$ *in white matter (WM) regions and* $5^o \pm 13^o$ *over the entire brain.*

Training the above-mentioned network using dMRI and AMBCA TOD data, however, resulted in over-fitting, potentially due to the residual mismatch between MRI and AMBCA TOD data, as well as noises and biases introduced during the generation of the AMBCA streamlines, which was not a complete representation of fiber orientation density within each voxel. In order to address this issue, we made the following changes: 1) we added one more layer, with a 1024-1024-1024-512-256 setting; 2) we included Parametric Rectified linear unit (PReLU) that picked the max value between a weighted and untouched current node output ($y = x$, when $x>0$; $y = ax$, when $x<0$; where a is a trainable parameter) to introduce nonlinear functions; 3) adding dropout as a

regularization method by randomly remove inputs during training (Srivastava et al. 2014; Demsar and Zupan 2021; Ying 2019), and the modified network is called TODNet. Fig. 1F shows the overall diagram of TODNet. In the first 1024-1024-1024 layers, 40% of the nodes were randomly dropped out to achieve converging training curve, and the last fully connected layer output TODs with a coefficient vector length of 28 (for a maximal harmonic order of 6). We also increased the training examples from 1 to 3 million patches.

During training, all other hyper-parameters were initialized using the parameters of the network trained using FODs. We employed the commonly used Adam's method (Duchi, Hazan, and Singer 2011) to stochastically optimize our loss function with some hyperparameters assigned before training: network weights initialization by truncated normal distribution centered on 0; initial learning rate = $1e^{-4}$, beta_1=0.9, beta_2=0.999, epsilon=$1e^{-08}$; Momentum = 0.5; Number of epochs = 1000; Batch size = 512. Early stopping was also employed by monitoring whether the validation set loss stabilized within 10 epochs to prevent overfitting (Zur et al. 2009). Similar to (Lin et al. 2019), our input dMRI data were normalized by dividing diffusion-weighted signals by non-diffusion-weighted signals. The trained models and codes are available at (https://github.com/liangzifei/MRTod_net). The output of the TODNet was called deep learning TODs (DL-TODs).

2.6. Tractography

Whole brain and region-of-interest (ROI)-based probabilistic tractography were performed using the tckgen command with the FOD2 option in MRtrix (v 3.0.3) using the optimized parameters reported in (Aydogan et al. 2018).

2.7. Statistical analysis

Two-sample *t*-test was used to test whether there was significant angular between the angular difference between AMBCA TODs and FODs/DL-TODs from dMRI. Two-sample *t*-test was also used to test whether there was significant difference in DICE between tracer projection areas and FOD/DL-TOD tractography results.

3. Results

3.1 The whole brain tracer streamline dataset

The AMBCA streamlines, by including data from multiple injection experiments, visualized the dense axonal pathways throughout the mouse forebrain. Major white matter tracts, such as the corpus callosum, anterior commissure, can be delineated in the dataset (Fig. 2A). Coherently arranged streamlines were also found in gray matter regions (e.g. cortex and hippocampus), reflecting axonal pathways in those regions, which are often challenging to reconstruct using dMRI tractography.

The AMBCA streamline dataset was a superset of streamlines from individual experiments. It is therefore not unexpected that, when compared to streamlines from individual experiment, selected AMBCA streamlines that passed through the same injection region tended to include additional streamlines reaching more extensive brain regions (Fig. 2B-C). These additional streamlines came from three sources: (1) inclusion of both anterograde streamlines originated from the injection region and retrograde streamlines originated from other regions but ended in the injection region; (2) inclusion of streamlines that merely passed through the injection region but did not originate or end there; (3) variations in streamlines observed in individual injection experiments, which reflected individual as well as inter-experimental variations, became less obvious in the collected AMBCA streamlines. Comparisons between the AMBCA streamline dataset and data from the MouseLight project (Winnubst et al. 2019), which traced long range axonal projections, did not show missing axonal projections (Fig. 2B-C), suggesting the AMBCA streamline dataset included most of the forebrain axonal pathways.

3.2 A comparison of the AMBCA streamline data with dMRI tractograaphy

Remarkable differences were found between the AMBCA streamline dataset and dMRI tractography results from ex vivo mouse brains. With the same number of total streamlines (4 million), the AMBCA streamline density maps showed less gray and white matter contrasts than streamline density maps from the dMRI tractography results (Fig. 2D), suggesting the dMRI tractography streamlines tended to stay within white matter regions. The overall contrast pattern found in the AMBCA streamline density

map resembled neurofilament stained histological sections (Fig. 2D), in which signal intensities reflect axonal density. In addition, the AMBCA streamlines tend to be longer than dMRI tractography streamlines (Fig. 2E).

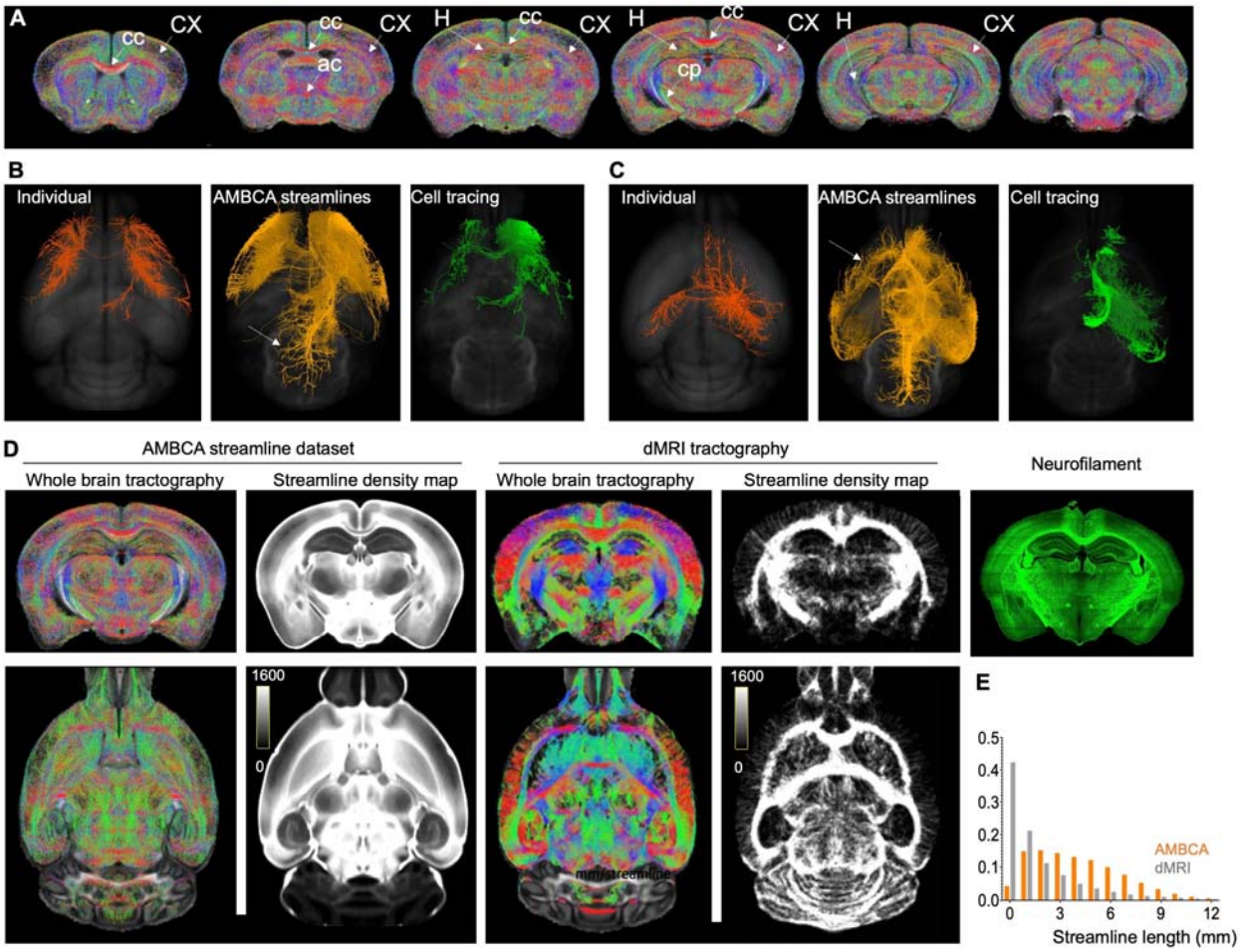

Fig. 2: *Axonal pathways in the AMBCA streamline data and comparisons with dMRI tractography.* ***A:*** *Axonal networks in the mouse brain shown in serial coronal sections of the AMBCA streamline data. Abbreviations are: ac: anterior commissure; cc: corpus callosum; cp: cerebral peduncle; CX: cortex; H: hippocampus.* ***B-C:*** *A comparison of streamlines originated from an injection site in the frontal cortex (B) and hippocampus (C) based on individual experiment, streamlines in the AMBCA streamline dataset that passed the injection site, and cell tracing data that pass the injection site. The arrows indicate the additional streamlines found in the AMBCA streamline dataset.* ***D:*** *Comparisons of AMBCA and dMRI tractography and corresponding streamline density maps, with a matching Neurofilament-M stained section from*

the Allen reference atlas. ***E:*** *The histograms of the lengths of streamline in the AMBCA dataset and dMRI tractography results.*

3.3 TODNet can predict tracer streamline TOD

As expected, the DL-TOD maps generated by the TODNet based on dMRI data from the test group resembled the AMBCA TOD maps (Fig. 3A). We measured the differences in the primary orientation (the orientation of the lobe with the highest amplitude) between DL-TODs and AMBCA TODs and between FODs and AMBCA TODs at each voxel in each subject space (Fig. 3B). In white matter regions, DL-TODs were slightly better aligned to the AMBCA TODs than FODs (8.54^o vs 12.94^o, $p<0.0001$, n=4). In gray matter regions, DL-TODs showed a much smaller angular difference compared to AMBCA TODs than FODs (Fig. 3C; 35.24^o vs 53.16^o, $p<0.0001$, n=4), notably in the cortex and hippocampus (Fig. 3B).

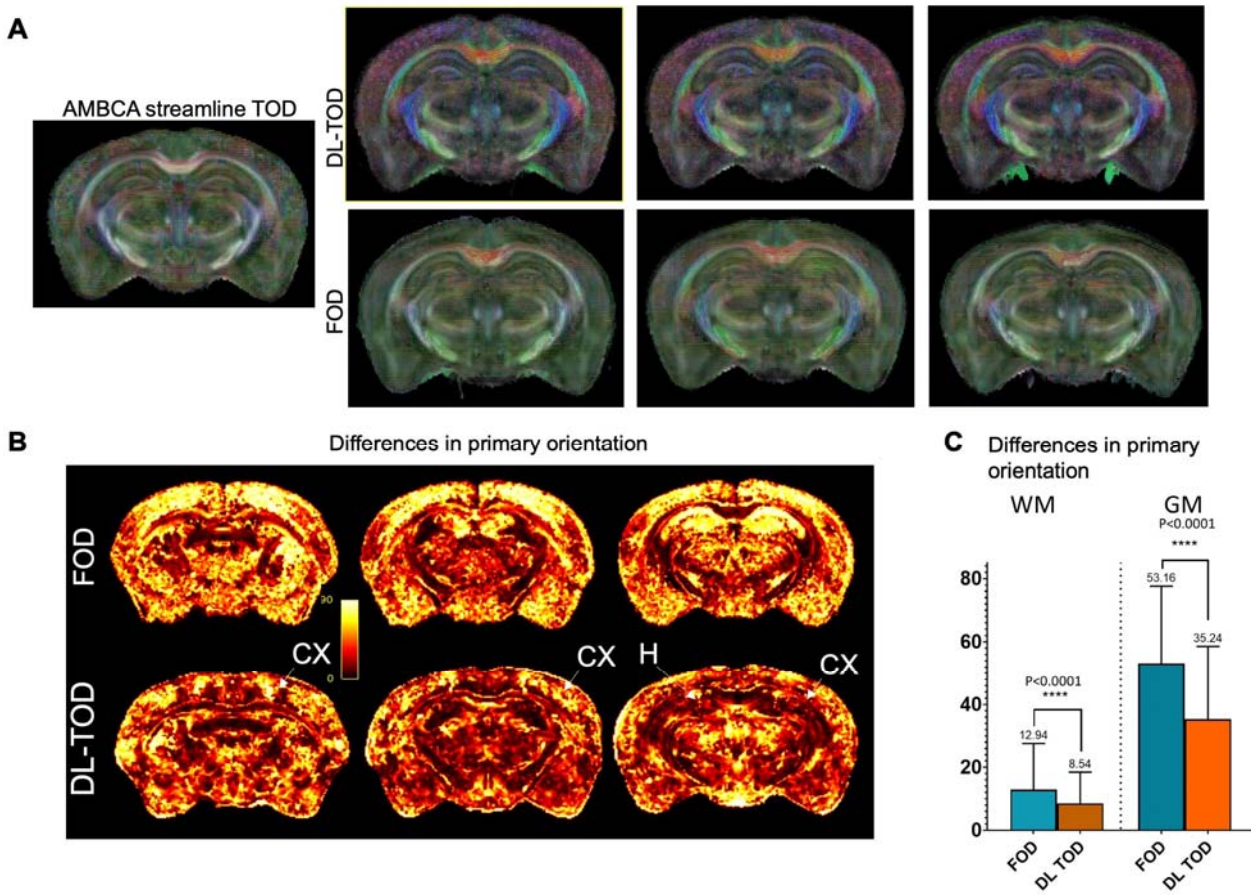

Fig. 3: *Comparisons of DL-TOD and conventional FOD.* ***A:*** *The estimated DL-TOD and FOD maps from three mouse brains not included in training.* ***B:*** *The differences in the primary orientation between the DL-TODs and AMBCA TODs and between the FODs and AMBCA TODs. Notice the reductions in primary orientation differences in the cortex (CX) and hippocampus (H) in the DL-TOD results compared to the FOD results.* ***C:*** *Differences in primary orientation in white matter (WM) and gray matter (GM).*

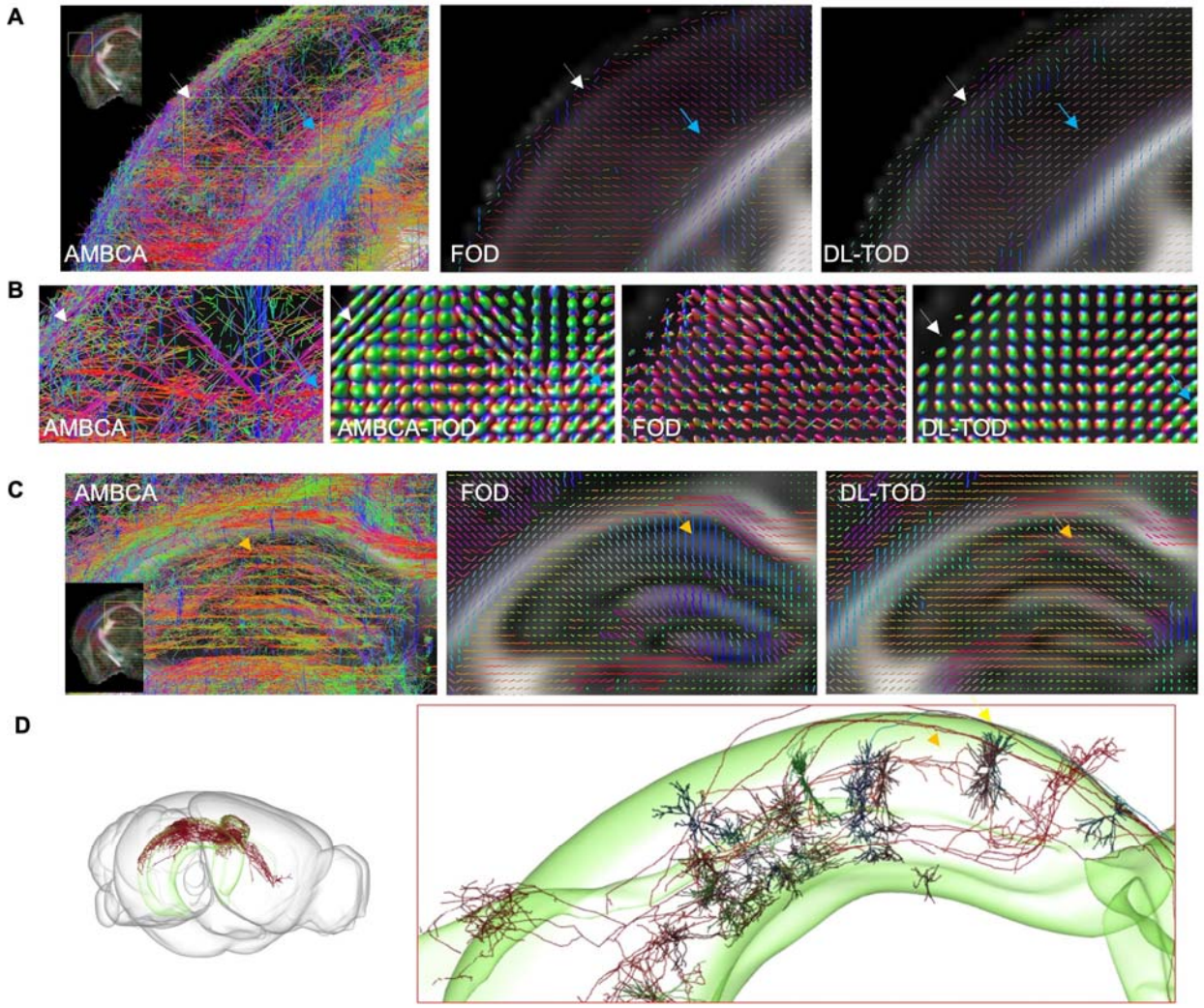

Fig. 4: *DL-TOD maps recapitulated axonal networks in the cortex and hippocampus.* ***A:*** *AMBCA streamlines in the sensory cortex (its location is shown in the insert) were compared with the primary orientations of FODs and DL-TODs. The white and blue arrows indicate the superficial and deep region of the cortex, where the primary orientation of FODs and DL-TODs differed.* ***B:*** *AMBCA TODs were compared with FODs and DL-TODs in the same region.* ***C:*** *AMBCA streamlines in the dorsal hippocampus (its location is shown in the insert) were compared with*

the primary orientations of FODs and DL-TODs. The orange arrow indicates a region in the dorsal hippocampus, where the primary orientation of FODs and DL-TODs differed. ***D:*** *Rendering of axons (deep red) and dendrites (dark green) of a few selected neurons in the hippocampus from the MouseLight project (Winnubst et al. 2019).*

In the sensory cortex, the AMBCA streamline dataset showed tangential streamlines (parallel to the cortical surface) in regions near the surface and base of the cortex, which was reproduced by the primary orientations of DL-TODs, but the primary orientation of FODs generated by spherical deconvolution showed a rather uniform radial organization (Fig. 4A-B). In the hippocampus, the AMBCA streamlines mostly ran mediolaterally, perpendicular to the primary orientations of FODs in the region, whereas the primary orientations of DL-TODs mostly agreed with the AMBCA streamline data (Fig. 4C). Single cell tracing data showed dense dendritic network in the hippocampus (short dark branches in Fig. 4D), along the primary directions of FODs, whereas axons of the same neurons (dark red streamlines in Fig. 4B) followed similar trajectories as shown by the AMBCA streamlines.

3.4 DL-TOD based tractography in the mouse brain

We then examined whether DL-TOD was able to improve tractography in the mouse brain. Using a set of 10 injection regions in the AMBCA, streamlines were selected from the AMBCA streamline dataset and tractography results based on FODs and DL-TODs. Notice the AMBCA streamlines selected included all streamlines that passed through the regions, not just the streamlines from individual injection experiments. Fig. 5A-C show the selected streamlines that passed through injection regions in the frontal cortex, thalamus, and hippocampus, overlaid on horizontal and axial FA images. Visually, tractography results based on DL-TODs agreed with the AMBCA streamlines better than tractography results based on FODs. Fig. 5D shows streamlines from three experiments in AMBCA with injection sites in different part of the hippocampus. Streamlines generated by tractography based on DL-TODs again showed a good agreement with the AMBCA results, whereas streamlines generated by FOD-based

tractography tended to be shorter, and in the case of a region in the dentate gyrus (red streamlines), followed a different path than the AMBCA streamlines.

We used the dice index to measure spatial agreements between tractography results based on either FOD or DL-TOD from 10 injection regions in AMBCA and the corresponding AMBCA streamlines selected using the same regions (Fig. 5E). The DL-TOD results had significantly higher DICE scores than FOD in 7 out of the 10 cases and comparable DICE scores for the rest. Further analysis showed that DL-TOD based tractography improved specificity by reducing over-reach, while mostly maintaining the same level of sensitivity or overlap compared to FOD-based tractography (Fig. 5F). Among the 10 regions, however, DL-TOD tractography from one region in the cortex (ID# 309372716) showed a large drop in sensitivity compared to FOD tractography.

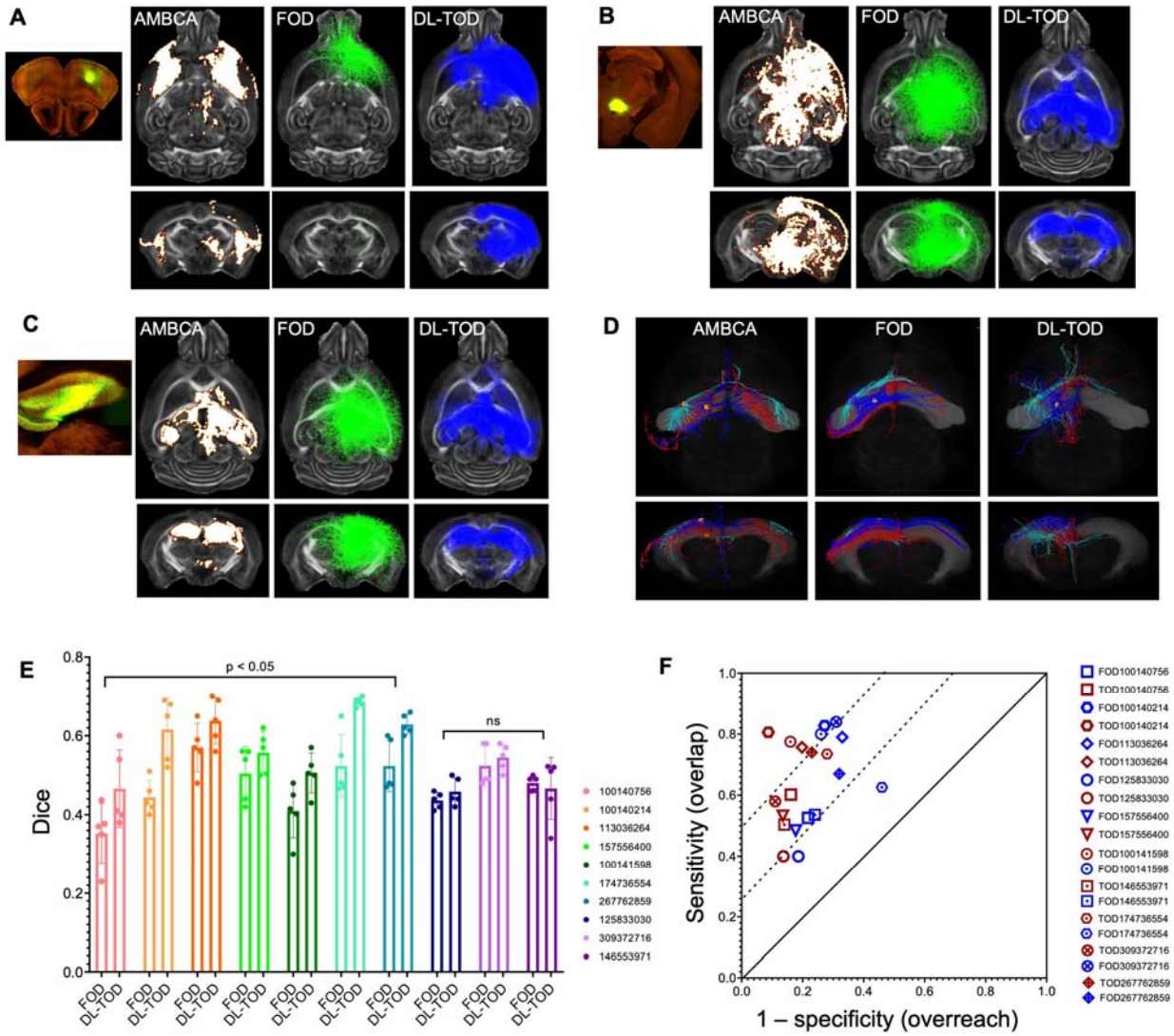

Fig. 5: *DL-TODs improved dMRI tractography in the mouse brain.* ***A-C:*** *Comparisons of streamlines selected from the AMBCA streamline dataset and FOD/DL-TOD based tractography using injection regions in the frontal cortex (A), thalamus (B), and hippocampus (C).* ***D:*** *Comparisons of axonal pathways from three injection sites in the mouse hippocampus in the AMBCA with FOD and DL-TOD based tractography from the same injection sites.* ***E:*** *Spatial overlaps between streamlines selected from the AMBCA streamline dataset and FOD/DL-TOD based tractography using 10 injection sites in AMBCA measured using DICE.* ***F:*** *For the results in E, DL-TOD based tractography results tended to have higher specificity (smaller over-reach) than FOD based tractography results while maintaining similar sensitivity (overlap).*

3.5 Potential effects of streamline distribution in AMBCA on DL-TOD

Based on the dMRI signals in the corpus callosum, we simulated dMRI signals from orthogonal crossing fibers, as shown by the estimated FODs from the simulated dMRI signals (Fig. 6A). In the six-by-six matrix, FODs in the diagonal elements showed two lobes with equal amplitudes, representing the crossing of two equivalent groups of fibers, and FODs along the upper or left edge only had one lobe, representing voxels with a single group of fibers, with everything else in between. The estimated DL-TODs from the simulated dMRI signals showed less sharply defined lobes than FODs (Fig 6A). When fibers along the x axis (left-right in the mouse brain) were mixed with fibers along the z axis (rostral-caudal in the mouse brain), the estimated DL-TODs showed more preference for the x axis than the z axis, as the DL-TODs in the diagonal elements have their primarily orientations along the x axis. When fibers along the x axis were mixed with fibers along the y axis (dorsal-ventral in the mouse brain), the estimated DL-TODs showed more preference for the y axis than the x axis.

The preference toward certain orientations in the DL-TODs might reflect the distribution of orientation in the AMBCA streamline dataset. When we projected the orientation of each streamline segment onto the x, y, and z axes, the projections along the y axis out-numbered the projections along the other two axes (Fig. 6B), which might have caused the tilt toward the y axis, followed by the x axis, of DL-TODs. Furthermore, examinations of the angles between each streamline segments and the x/y/z axis showed that, among the streamline segments that closely aligned with the x, y, and z axes (angle $<10^{o}$), more streamlines segments were closely aligned with the x axis than the y and z axes (Fig. 6C). This might explain why the DL-TODs in the simulation were sharper for fiber groups along the x axis than others.

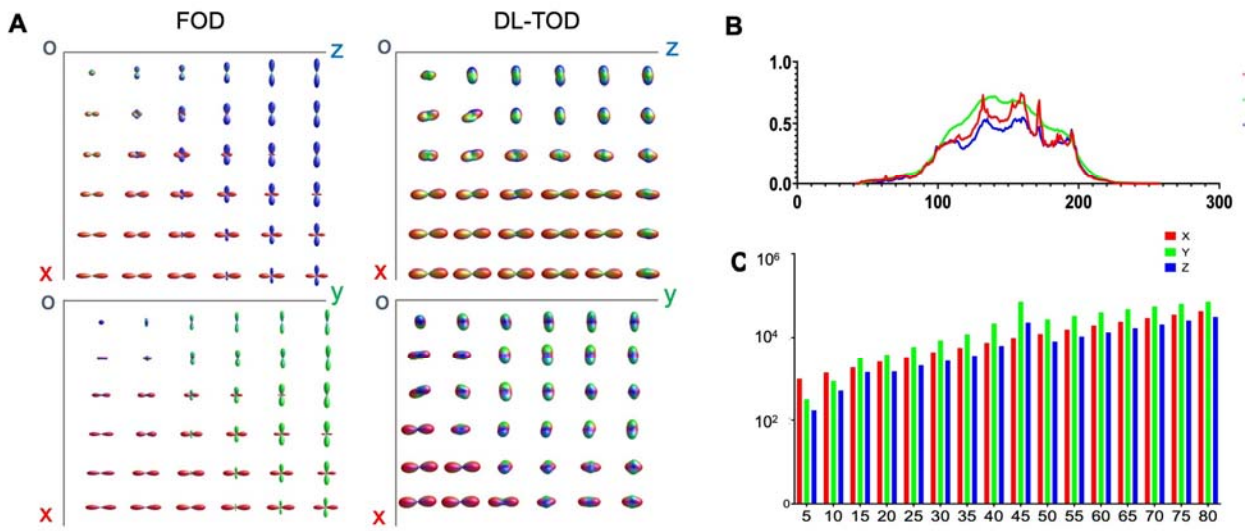

Fig. 6: Comparing FODs and TODs in a digital phantom and potential bias in the AMBCA streamline database. A: In a digital phantom with single and orthogonal crossing fibers (top: x and y; bottom: x and z). The dMRI signals from each fiber group were generated using the diffusion tensor model with diagonal elements filled with axial and radial diffusivity values from the corpus callosum of the ex vivo mouse brain dMRI data. By adjusting the proportions of each fiber group, the dMRI signals of voxels with single or crossing fibers were generated, and estimated FODs and DL-TODs were displayed here. **B:** The total projection of all AMBCA streamline segments along the x, y, and z axes in each axial slice. **C:** The distributions of angles between AMBCA streamline segments and the three axes.

4. Discussion

4.1 The advantages and limitations of the whole brain tracer streamline dataset

Previous studies on validation and optimization of dMRI tractography mostly used individual experiments as ground truth (Mollink et al. 2017; Schilling et al. 2016; Schilling et al. 2018) as it is technically challenging and time consuming to obtain comprehensive tracing data for the entire brain. For example, the connectome of the adult drosophila brain was completed only recently (Scheffer et al. 2020). As dMRI tractography cannot distinguish anterograde from retrograde connections or axons merely passing a region from those that originate from or end in it, the AMBCA streamline dataset, which contains streamlines from multiple experiments, may be more suitable for validation and optimization of dMRI tractography in the mouse brain than

results from individual experiments. Even though the streamlines and dMRI data were not from the same subject, which is not ideal as suggested by previous studies (Grisot, Haber, and Yendiki 2021), the inter-subject differences are expected to be small among the inbred C57BL mouse brains, especially with more than 2,700 subject data included in the AMBCA streamline dataset.

The AMBCA streamline dataset, however, remained an incomplete representation of the axonal networks in the mouse brain due to limitations in several aspects, including non-uniform distribution of injection sites, varying dosages and labelling efficiency, imaging resolution, and the fast marching algorithm. For example, as the cerebellum received fewer injections than the cortex, the density of streamlines in the cerebellum was noticeably lower than in the forebrain as shown in Fig. 2D. The orientations of TODs, however, reflected those of actual axonal pathways. Due to this reason, the amplitudes of the AMBCA TODs were normalized so that mainly the orientation information from the AMBCA TODs were used for training the deep learning network. This limitation may be alleviated with more tract and cell tracing resources in the future (e.g. (Winnubst et al. 2019; Zingg et al. 2014)). It is also not clear whether the technique developed using the AMBCA streamline dataset can be translated to data from the human brain, due to the vast differences in imaging resolution as well as differences in microstructural organization. The recent reports of tract tracing in non-human primate brain (Charvet et al. 2022; Xu et al. 2021; Howard et al. 2019) offer hope that such data, which have higher translational value, may become more readily available in the future.

4.2. Deep learning can enhance the accuracy in FOD estimation.

The deep learning framework has several advantages that complement existing modeling approaches, as it is data-driven and not limited by underlying assumptions associated with models. Here, we trained out network using small 3x3x3 patches instead of entire images because we assumed the relationship between dMRI signals and underlying axonal pathways to be strictly local (i.e. MRI signals are the ensemble average of spins within each voxel and do not depend on neighboring voxels) and would like to limit the amount of spatial information available to the network, in a similar

fashion as our previous study connecting MRI signals and histology (Liang et al. 2022). As a result, a limited number of typical dMRI data, instead of thousands as required in typical deep learning studies, can provides sufficient instances to train the deep learning network to resolve the orientation of certain axonal pathways in gray matter. The network can be extended to include dMRI data acquired using optimized parameters or other MRI contrasts to further enhance its capability. For example, the recent developments on the multi-dimensional diffusion encoding (Topgaard 2017) may provide critical information on tissue microstructural organization that can be utilized by the network.

Our results demonstrated that deep learning networks, trained with histological ground truth, were able to enhance the accuracy in estimating axonal fiber orientation (Fig. 4) and improve tractography results (Fig. 5) in the mouse brain. The improvements were most obvious in gray matter regions (Fig. 3B-C) since conventional FOD estimates are already fairly accurate in depicting the orientation of white matter bundles (Schilling et al. 2018; Mollink et al. 2017; Lin et al. 2001). The complex microstructural organization in gray matter, with the presence of the dendritic network and other cellular compartments, however, challenges the power of dMRI in resolving axonal pathways in gray matter regions, as shown previously in the mouse hippocampus (Wu and Zhang 2016) and other regions (Ren et al. 2007; Moldrich et al. 2010; Wu et al. 2014). The deep learning network developed here, as shown in Fig. 5D, may be used to reconstruct structural connectivity in the mouse hippocampus or other regions.

One limitation of the deep learning approach is that biases in the training data will influence the network predictions. The mouse brain has a higher relative gray matter volume than the human brain. In addition, the distribution of streamlines' orientation, as shown in Fig. 6B, was not uniform, which may reflect actual axonal organization in the brain (i.e. more axons running horizontally than axons running vertically) or may be a result of the atlas space used here. In the future, training datasets containing with equalized tissue types and multiple orientations may be able to reduce the bias.

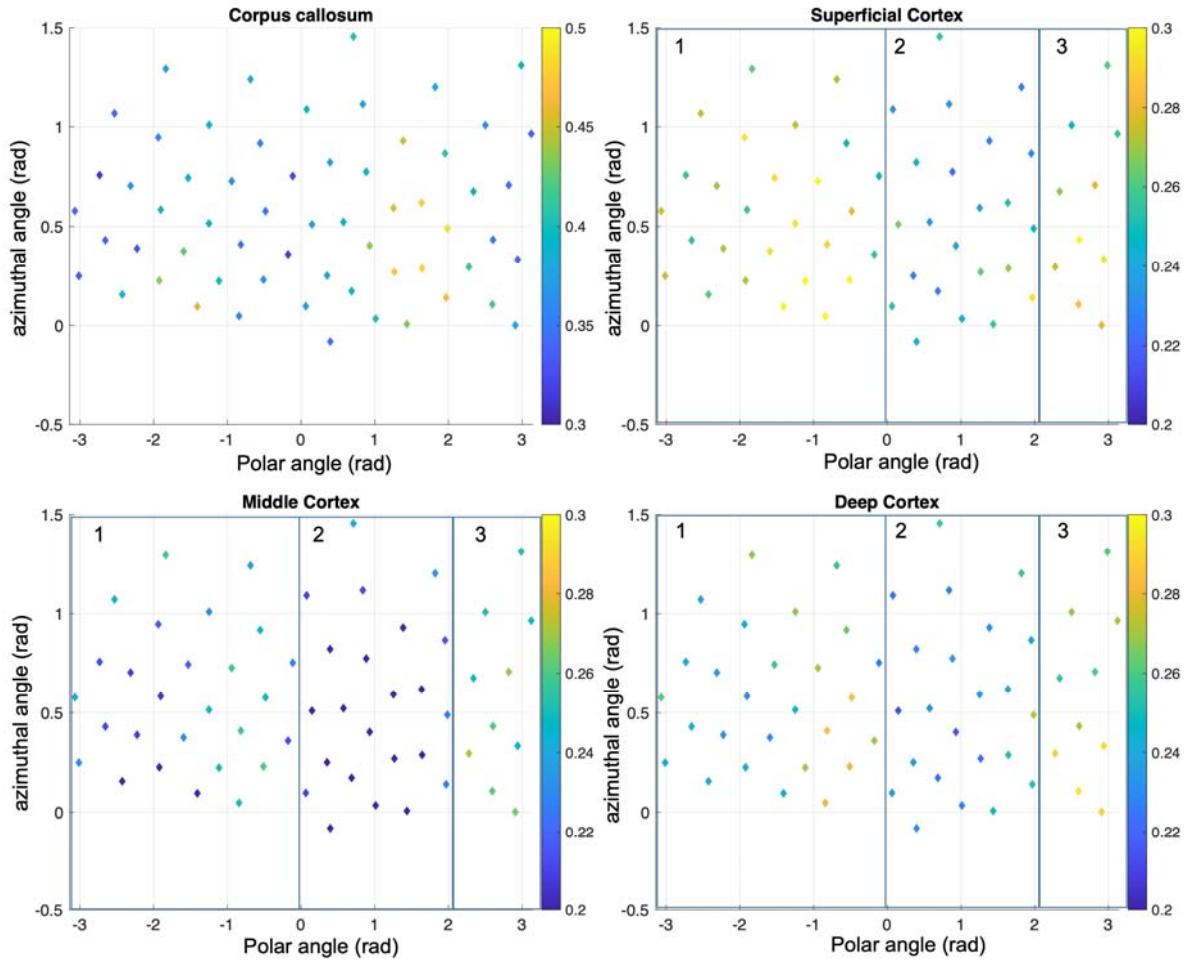

Fig. 7: *Normalized dMRI signals from representative voxels in the corpus callosum, superficial, middle, and deep cortical regions. The locations of the signals in the plot indicate the polar and azimuthal angles of the corresponding diffusion encoding gradient, and the color indicates the normalized signal strength (with respect to non-diffusion-weighted signals). The plots of cortical dMRI signals are overlaid with three rectangular boxes to guide visual comparisons.*

Our results also did not provide detailed knowledge of the inner working of the network. For example, it is intriguing that the network was able to assign distinct orientations to the superficial, middle, and deep cortical regions based on dMRI signals (Fig. 4A). The normalized dMRI signals in these three regions and corpus callosum are displayed in Fig. 7. The dMRI signals in the corpus callosum had less attenuations than signals from the three cortical regions, and strong signal attenuations were observed when the diffusion encoding gradients were close to the left-right direction (polar angle

close to 0 and $\pm\pi$ in the plot). The dMRI signals from the three cortical regions all showed more attenuations than the corpus callosum but displayed different patterns. All three regions showed more attenuations in region 2 in Fig. 7, but the superficial and deep cortical regions had less attenuation than the middle cortical region in region 2, and much less attenuation in regions 1 and 3, potentially due to crossing fibers. The deep learning network might have recognized the differences in dMRI signals among the three regions and used the information to predict the DL-TOD, whereas the conventional spherical deconvolution using response functions derived from white matter regions did not resolve the crossing fibers accurately in this case.

In summary, we demonstrated that a deep learning network, trained using the AMBCA streamline dataset, can improve the estimation of fiber orientations as well as the specificity of tractography results from mouse brain dMRI data. The technique developed here can be used to characterize structural connectivity in the mouse brain.

References

Aggarwal, M., S. Mori, T. Shimogori, S. Blackshaw, and J. Y. Zhang. 2010. 'Three-Dimensional Diffusion Tensor Microimaging for Anatomical Characterization of the Mouse Brain', *Magnetic Resonance in Medicine*, 64: 249-61.

Arefin, T. M., C. H. Lee, J. D. White, J. Zhang, and A. Kaffman. 2021. 'Macroscopic Structural and Connectome Mapping of the Mouse Brain Using Diffusion Magnetic Resonance Imaging', *Bio Protoc*, 11: e4221.

Aydogan, D. B., R. Jacobs, S. Dulawa, S. L. Thompson, M. C. Francois, A. W. Toga, H. W. Dong, J. A. Knowles, and Y. G. Shi. 2018. 'When tractography meets tracer injections: a systematic study of trends and variation sources of diffusion-based connectivity', *Brain Structure & Function*, 223: 2841-58.

Azadbakht, H., L. M. Parkes, H. A. Haroon, M. Augath, N. K. Logothetis, A. de Crespigny, H. E. D'Arceuil, and G. J. M. Parker. 2015. 'Validation of High-

Resolution Tractography Against In Vivo Tracing in the Macaque Visual Cortex', *Cerebral Cortex*, 25: 4299-309.

Basser, P. J., and D. K. Jones. 2002. 'Diffusion-tensor MRI: theory, experimental design and data analysis - a technical review', *NMR Biomed*, 15: 456-67.

Behrens, T. E., H. J. Berg, S. Jbabdi, M. F. Rushworth, and M. W. Woolrich. 2007. 'Probabilistic diffusion tractography with multiple fibre orientations: What can we gain?', *Neuroimage*, 34: 144-55.

Calabrese, E., A. Badea, C. L. Coe, G. R. Lubach, M. A. Styner, and G. A. Johnson. 2014. 'Investigating the Tradeoffs Between Spatial Resolution and Diffusion Sampling for Brain Mapping with Diffusion Tractography: Time Well Spent?', *Human Brain Mapping*, 35: 5667-85.

Calabrese, M., R. Magliozzi, O. Ciccarelli, J. J. G. Geurts, R. Reynolds, and R. Martin. 2015. 'Exploring the origins of grey matter damage in multiple sclerosis', *Nature Reviews Neuroscience*, 16: 147-58.

Catani, M., R. J. Howard, S. Pajevic, and D. K. Jones. 2002. 'Virtual in vivo interactive dissection of white matter fasciculi in the human brain', *Neuroimage*, 17: 77-94.

Ceritoglu, C., K. Oishi, X. Li, M. C. Chou, L. Younes, M. Albert, C. Lyketsos, P. C. van Zijl, M. I. Miller, and S. Mori. 2009. 'Multi-contrast large deformation diffeomorphic metric mapping for diffusion tensor imaging', *Neuroimage*, 47: 618-27.

Charvet, C. J., K. Ofori, C. Baucum, J. Sun, M. S. Modrell, K. Hekmatyar, B. L. Edlow, and A. J. van der Kouwe. 2022. 'Tracing Modification to Cortical Circuits in Human and Nonhuman Primates from High-Resolution Tractography, Transcription, and Temporal Dimensions', *J Neurosci*, 42: 3749-67.

Chen, H., T. Liu, Y. Zhao, T. Zhang, Y. Li, M. Li, H. Zhang, H. Kuang, L. Guo, J. Z. Tsien, and T. Liu. 2015. 'Optimization of large-scale mouse brain connectome via joint evaluation of DTI and neuron tracing data', *Neuroimage*, 115: 202-13.

Demsar, J., and B. Zupan. 2021. 'Hands-on training about overfitting', *Plos Computational Biology*, 17.

Dhollander, T., L. Emsell, W. Van Hecke, F. Maes, S. Sunaert, and P. Suetens. 2014. 'Track orientation density imaging (TODI) and track orientation distribution (TOD) based tractography', *Neuroimage*, 94: 312-36.

Duchi, J., E. Hazan, and Y. Singer. 2011. 'Adaptive Subgradient Methods for Online Learning and Stochastic Optimization', *Journal of Machine Learning Research*, 12: 2121-59.

Dyrby, T. B., L. V. Sogaard, G. J. Parker, D. C. Alexander, N. M. Lind, W. F. Baare, A. Hay-Schmidt, N. Eriksen, B. Pakkenberg, O. B. Paulson, and J. Jelsing. 2007. 'Validation of in vitro probabilistic tractography', *Neuroimage*, 37: 1267-77.

Fillard, P., M. Descoteaux, A. Goh, S. Gouttard, B. Jeurissen, J. Malcolm, A. Ramirez-Manzanares, M. Reisert, K. Sakaie, F. Tensaouti, T. Yo, J. F. Mangin, and C. Poupon. 2011. 'Quantitative evaluation of 10 tractography algorithms on a realistic diffusion MR phantom', *Neuroimage*, 56: 220-34.

Frank, L. R. 2001. 'Anisotropy in high angular resolution diffusion-weighted MRI', *Magn Reson Med*, 45: 935-9.

Gibbons, E. K., K. K. Hodgson, A. S. Chaudhari, L. G. Richards, J. J. Majersik, G. Adluru, and E. V. R. DiBella. 2019. 'Simultaneous NODDI and GFA parameter map generation from subsampled q-space imaging using deep learning', *Magn Reson Med*, 81: 2399-411.

Grisot, G., S. N. Haber, and A. Yendiki. 2021. 'Diffusion MRI and anatomic tracing in the same brain reveal common failure modes of tractography', *Neuroimage*, 239.

Gutierrez, C. E., H. Skibbe, K. Nakae, H. Tsukada, J. Lienard, A. Watakabe, J. Hata, M. Reisert, A. Woodward, Y. Yamaguchi, T. Yamamori, H. Okano, S. Ishii, and K. Doya. 2020. 'Optimization and validation of diffusion MRI-based fiber tracking with neural tracer data as a reference', *Scientific Reports*, 10.

Howard, A. F., J. Mollink, M. Kleinnijenhuis, M. Pallebage-Gamarallage, M. Bastiani, M. Cottaar, K. L. Miller, and S. Jbabdi. 2019. 'Joint modelling of diffusion MRI and microscopy', *Neuroimage*, 201: 116014.

Jbabdi, S., and H. Johansen-Berg. 2011. 'Tractography: where do we go from here?', *Brain Connect*, 1: 169-83.

Jbabdi, S., S. N. Sotiropoulos, S. N. Haber, D. C. Van Essen, and T. E. Behrens. 2015. 'Measuring macroscopic brain connections in vivo', *Nat Neurosci*, 18: 1546-55.

Jones, D. K., T. R. Knosche, and R. Turner. 2013. 'White matter integrity, fiber count, and other fallacies: the do's and don'ts of diffusion MRI', *Neuroimage*, 73: 239-54.

Jones, R., G. Grisot, J. Augustinack, C. Magnain, D. A. Boas, B. Fischl, H. Wang, and A. Yendiki. 2020. 'Insight into the fundamental trade-offs of diffusion MRI from polarization -sensitive optical coherence tomography in ex vivo human brain', *Neuroimage*, 214.

Kuan, L., Y. Li, C. Lau, D. Feng, A. Bernard, S. M. Sunkin, H. Zeng, C. Dang, M. Hawrylycz, and L. Ng. 2015. 'Neuroinformatics of the Allen Mouse Brain Connectivity Atlas', *Methods*, 73: 4-17.

Lein, E. S., M. J. Hawrylycz, N. Ao, M. Ayres, A. Bensinger, A. Bernard, A. F. Boe, M. S. Boguski, K. S. Brockway, E. J. Byrnes, L. Chen, L. Chen, T. M. Chen, M. C. Chin, J. Chong, B. E. Crook, A. Czaplinska, C. N. Dang, S. Datta, N. R. Dee, A. L. Desaki, T. Desta, E. Diep, T. A. Dolbeare, M. J. Donelan, H. W. Dong, J. G. Dougherty, B. J. Duncan, A. J. Ebbert, G. Eichele, L. K. Estin, C. Faber, B. A. Facer, R. Fields, S. R. Fischer, T. P. Fliss, C. Frensley, S. N. Gates, K. J. Glattfelder, K. R. Halverson, M. R. Hart, J. G. Hohmann, M. P. Howell, D. P. Jeung, R. A. Johnson, P. T. Karr, R. Kawal, J. M. Kidney, R. H. Knapik, C. L. Kuan, J. H. Lake, A. R. Laramee, K. D. Larsen, C. Lau, T. A. Lemon, A. J. Liang, Y. Liu, L. T. Luong, J. Michaels, J. J. Morgan, R. J. Morgan, M. T. Mortrud, N. F. Mosqueda, L. L. Ng, R. Ng, G. J. Orta, C. C. Overly, T. H. Pak, S. E. Parry, S. D. Pathak, O. C. Pearson, R. B. Puchalski, Z. L. Riley, H. R. Rockett, S. A. Rowland, J. J. Royall, M. J. Ruiz, N. R. Sarno, K. Schaffnit, N. V. Shapovalova, T. Sivisay, C. R. Slaughterbeck, S. C. Smith, K. A. Smith, B. I. Smith, A. J. Sodt, N. N. Stewart, K. R. Stumpf, S. M. Sunkin, M. Sutram, A. Tam, C. D. Teemer, C. Thaller, C. L. Thompson, L. R. Varnam, A. Visel, R. M. Whitlock, P. E. Wohnoutka, C. K. Wolkey, V. Y. Wong, M. Wood, M. B. Yaylaoglu, R. C. Young, B. L. Youngstrom, X. F. Yuan, B. Zhang, T. A. Zwingman, and A. R. Jones. 2007. 'Genome-wide atlas of gene expression in the adult mouse brain', *Nature*, 445: 168-76.

Li, H., Z. Liang, C. Zhang, R. Liu, J. Li, W. Zhang, D. Liang, B. Shen, X. Zhang, Y. Ge, J. Zhang, and L. Ying. 2021. 'SuperDTI: Ultrafast DTI and fiber tractography with deep learning', *Magn Reson Med*, 86: 3334-47.

Liang, Z., C. H. Lee, T. M. Arefin, Z. Dong, P. Walczak, S. H. Shi, F. Knoll, Y. Ge, L. Ying, and J. Zhang. 2022. 'Virtual mouse brain histology from multi-contrast MRI via deep learning', *Elife*, 11.

Liebrand, L. C., G. A. van Wingen, F. M. Vos, D. Denys, and M. W. A. Caan. 2020. 'Spatial versus angular resolution for tractography-assisted planning of deep brain stimulation', *Neuroimage Clin*, 25: 102116.

Lim, I. A. L., A. V. Faria, X. Li, J. T. C. Hsu, R. D. Airan, S. Mori, and P. C. M. van Ziji. 2013. 'Human brain atlas for automated region of interest selection in quantitative susceptibility mapping: Application to determine iron content in deep gray matter structures', *Neuroimage*, 82: 449-69.

Lin, C. P., W. Y. I. Tseng, H. C. Cheng, and J. H. Chen. 2001. 'Validation of diffusion tensor magnetic resonance axonal fiber imaging with registered manganese-enhanced optic tracts', *Neuroimage*, 14: 1035-47.

Lin, Z., T. Gong, K. Wang, Z. Li, H. He, Q. Tong, F. Yu, and J. Zhong. 2019. 'Fast learning of fiber orientation distribution function for MR tractography using convolutional neural network', *Med Phys*, 46: 3101-16.

Lo, C. Y., P. N. Wang, K. H. Chou, J. Wang, Y. He, and C. P. Lin. 2010. 'Diffusion tensor tractography reveals abnormal topological organization in structural cortical networks in Alzheimer's disease', *J Neurosci*, 30: 16876-85.

Maier-Hein, K. H., P. F. Neher, J. C. Houde, M. A. Cote, E. Garyfallidis, J. Zhong, M. Chamberland, F. C. Yeh, Y. C. Lin, Q. Ji, W. E. Reddick, J. O. Glass, D. Q. Chen, Y. Feng, C. Gao, Y. Wu, J. Ma, R. He, Q. Li, C. F. Westin, S. Deslauriers-Gauthier, J. O. O. Gonzalez, M. Paquette, S. St-Jean, G. Girard, F. Rheault, J. Sidhu, C. M. W. Tax, F. Guo, H. Y. Mesri, S. David, M. Froeling, A. M. Heemskerk, A. Leemans, A. Bore, B. Pinsard, C. Bedetti, M. Desrosiers, S. Brambati, J. Doyon, A. Sarica, R. Vasta, A. Cerasa, A. Quattrone, J. Yeatman, A. R. Khan, W. Hodges, S. Alexander, D. Romascano, M. Barakovic, A. Auria, O. Esteban, A. Lemkaddem, J. P. Thiran, H. E. Cetingul, B. L. Odry, B. Mailhe, M.

S. Nadar, F. Pizzagalli, G. Prasad, J. E. Villalon-Reina, J. Galvis, P. M. Thompson, F. S. Requejo, P. L. Laguna, L. M. Lacerda, R. Barrett, F. Dell'Acqua, M. Catani, L. Petit, E. Caruyer, A. Daducci, T. B. Dyrby, T. Holland-Letz, C. C. Hilgetag, B. Stieltjes, and M. Descoteaux. 2017. 'The challenge of mapping the human connectome based on diffusion tractography', *Nat Commun*, 8: 1349.

Moldrich, R. X., K. Pannek, R. Hoch, J. L. Rubenstein, N. D. Kurniawan, and L. J. Richards. 2010. 'Comparative mouse brain tractography of diffusion magnetic resonance imaging', *Neuroimage*, 51: 1027-36.

Mollink, J., M. Kleinnijenhuis, A. V. Cappellen van Walsum, S. N. Sotiropoulos, M. Cottaar, C. Mirfin, M. P. Heinrich, M. Jenkinson, M. Pallebage-Gamarallage, O. Ansorge, S. Jbabdi, and K. L. Miller. 2017. 'Evaluating fibre orientation dispersion in white matter: Comparison of diffusion MRI, histology and polarized light imaging', *Neuroimage*, 157: 561-74.

Mori, S., and P. C. van Zijl. 2002. 'Fiber tracking: principles and strategies - a technical review', *NMR Biomed*, 15: 468-80.

Oh, S. W., J. A. Harris, L. Ng, B. Winslow, N. Cain, S. Mihalas, Q. X. Wang, C. Lau, L. Kuan, A. M. Henry, M. T. Mortrud, B. Ouellette, T. N. Nguyen, S. A. Sorensen, C. R. Slaughterbeck, W. Wakeman, Y. Li, D. Feng, A. Ho, E. Nicholas, K. E. Hirokawa, P. Bohn, K. M. Joines, H. C. Peng, M. J. Hawrylycz, J. W. Phillips, J. G. Hohmann, P. Wohnoutka, C. Koch, A. Bernard, C. Dang, A. R. Jones, H. K. Zeng, and C. R. Gerfen. 2014. 'A mesoscale connectome of the mouse brain', *Nature*, 508: 207-+.

Poot, D. H., B. Jeurissen, Y. Bastiaensen, J. Veraart, W. Van Hecke, P. M. Parizel, and J. Sijbers. 2013. 'Super-resolution for multislice diffusion tensor imaging', *Magn Reson Med*, 69: 103-13.

Ren, T., J. Zhang, C. Plachez, S. Mori, and L. J. Richards. 2007. 'Diffusion tensor magnetic resonance imaging and tract-tracing analysis of Probst bundle structure in Netrin1- and DCC-deficient mice', *J Neurosci*, 27: 10345-9.

Reveley, C., A. K. Seth, C. Pierpaoli, A. C. Silva, D. Yu, R. C. Saunders, D. A. Leopold, and F. Q. Ye. 2015. 'Superficial white matter fiber systems impede detection of

long-range cortical connections in diffusion MR tractography', *Proc Natl Acad Sci U S A*, 112: E2820-8.

Scheffer, L. K., C. S. Xu, M. Januszewski, Z. Lu, S. Y. Takemura, K. J. Hayworth, G. B. Huang, K. Shinomiya, J. Maitlin-Shepard, S. Berg, J. Clements, P. M. Hubbard, W. T. Katz, L. Umayam, T. Zhao, D. Ackerman, T. Blakely, J. Bogovic, T. Dolafi, D. Kainmueller, T. Kawase, K. A. Khairy, L. Leavitt, P. H. Li, L. Lindsey, N. Neubarth, D. J. Olbris, H. Otsuna, E. T. Trautman, M. Ito, A. S. Bates, J. Goldammer, T. Wolff, R. Svirskas, P. Schlegel, E. Neace, C. J. Knecht, C. X. Alvarado, D. A. Bailey, S. Ballinger, J. A. Borycz, B. S. Canino, N. Cheatham, M. Cook, M. Dreher, O. Duclos, B. Eubanks, K. Fairbanks, S. Finley, N. Forknall, A. Francis, G. P. Hopkins, E. M. Joyce, S. Kim, N. A. Kirk, J. Kovalyak, S. A. Lauchie, A. Lohff, C. Maldonado, E. A. Manley, S. McLin, C. Mooney, M. Ndama, O. Ogundeyi, N. Okeoma, C. Ordish, N. Padilla, C. M. Patrick, T. Paterson, E. E. Phillips, E. M. Phillips, N. Rampally, C. Ribeiro, M. K. Robertson, J. T. Rymer, S. M. Ryan, M. Sammons, A. K. Scott, A. L. Scott, A. Shinomiya, C. Smith, K. Smith, N. L. Smith, M. A. Sobeski, A. Suleiman, J. Swift, S. Takemura, I. Talebi, D. Tarnogorska, E. Tenshaw, T. Tokhi, J. J. Walsh, T. Yang, J. A. Horne, F. Li, R. Parekh, P. K. Rivlin, V. Jayaraman, M. Costa, G. S. Jefferis, K. Ito, S. Saalfeld, R. George, I. A. Meinertzhagen, G. M. Rubin, H. F. Hess, V. Jain, and S. M. Plaza. 2020. 'A connectome and analysis of the adult Drosophila central brain', *Elife*, 9.

Schilling, K. G., V. Janve, Y. Gao, I. Stepniewska, B. A. Landman, and A. W. Anderson. 2018. 'Histological validation of diffusion MRI fiber orientation distributions and dispersion', *Neuroimage*, 165: 200-21.

Schilling, K. G., V. Nath, C. Hansen, P. Parvathaneni, J. Blaber, Y. R. Gao, P. Neher, D. B. Aydogan, Y. G. Shi, M. Ocampo-Pineda, S. Schiavi, A. Daducci, G. Girard, M. Barakovic, J. Rafael-Patino, D. Romascano, G. Rensonnet, M. Pizzolato, A. Bates, E. Fischi, J. P. Thiran, E. J. Canales-Rodriguez, C. Huang, H. T. Zhu, L. M. Zhong, R. Cabeen, A. W. Toga, F. Rheault, G. Theaud, J. C. Houde, J. Sidhu, M. Chamberland, C. F. Westin, T. B. Dyrby, R. Verma, Y. Rathi, M. O. Irfanoglu, C. Thomas, C. Pierpaoli, M. Descoteaux, A. W. Anderson, and B. A. Landman.

2019. 'Limits to anatomical accuracy of diffusion tractography using modern approaches', *Neuroimage*, 185: 1-11.

Schilling, K., V. Janve, Y. Gao, I. Stepniewska, B. A. Landman, and A. W. Anderson. 2016. 'Comparison of 3D orientation distribution functions measured with confocal microscopy and diffusion MRI', *Neuroimage*, 129: 185-97.

Schurr, R., Y. R. Duan, A. M. Norcia, S. Ogawa, J. D. Yeatman, and A. A. Mezer. 2018. 'Tractography optimization using quantitative T1 mapping in the human optic radiation', *Neuroimage*, 181: 645-58.

Seehaus, A. K., A. Roebroeck, O. Chiry, D. S. Kim, I. Ronen, H. Bratzke, R. Goebel, and R. A. Galuske. 2013. 'Histological validation of DW-MRI tractography in human postmortem tissue', *Cereb Cortex*, 23: 442-50.

Srivastava, N., G. Hinton, A. Krizhevsky, I. Sutskever, and R. Salakhutdinov. 2014. 'Dropout: A Simple Way to Prevent Neural Networks from Overfitting', *Journal of Machine Learning Research*, 15: 1929-58.

Thomas, C., F. Q. Ye, M. O. Irfanoglu, P. Modi, K. S. Saleem, D. A. Leopold, and C. Pierpaoli. 2014. 'Anatomical accuracy of brain connections derived from diffusion MRI tractography is inherently limited', *Proceedings of the National Academy of Sciences of the United States of America*, 111: 16574-79.

Topgaard, D. 2017. 'Multidimensional diffusion MRI', *J Magn Reson*, 275: 98-113.

Tournier, J. D., F. Calamante, and A. Connelly. 2007. 'Robust determination of the fibre orientation distribution in diffusion MRI: Non-negativity constrained super-resolved spherical deconvolution', *Neuroimage*, 35: 1459-72.

Tournier, J. D., R. Smith, D. Raffelt, R. Tabbara, T. Dhollander, M. Pietsch, D. Christiaens, B. Jeurissen, C. H. Yeh, and A. Connelly. 2019. 'MRtrix3: A fast, flexible and open software framework for medical image processing and visualisation', *Neuroimage*, 202.

Tuch, D. S., T. G. Reese, M. R. Wiegell, N. Makris, J. W. Belliveau, and V. J. Wedeen. 2002. 'High angular resolution diffusion imaging reveals intravoxel white matter fiber heterogeneity', *Magn Reson Med*, 48: 577-82.

Wedeen, V. J., D. L. Rosene, R. P. Wang, G. P. Dai, F. Mortazavi, P. Hagmann, J. H. Kaas, and W. Y. I. Tseng. 2012. 'The Geometric Structure of the Brain Fiber Pathways', *Science*, 335: 1628-34.

Wedeen, V. J., R. P. Wang, J. D. Schmahmann, T. Benner, W. Y. Tseng, G. Dai, D. N. Pandya, P. Hagmann, H. D'Arceuil, and A. J. de Crespigny. 2008. 'Diffusion spectrum magnetic resonance imaging (DSI) tractography of crossing fibers', *Neuroimage*, 41: 1267-77.

White, J. D., T. M. Arefin, A. Pugliese, C. H. Lee, J. Gassen, J. Y. Zhang, and A. Kaffman. 2020. 'Early life stress causes sex-specific changes in adult fronto-limbic connectivity that differentially drive learning', *Elife*, 9.

Winnubst, J., E. Bas, T. A. Ferreira, Z. Wu, M. N. Economo, P. Edson, B. J. Arthur, C. Bruns, K. Rokicki, D. Schauder, D. J. Olbris, S. D. Murphy, D. G. Ackerman, C. Arshadi, P. Baldwin, R. Blake, A. Elsayed, M. Hasan, D. Ramirez, B. Dos Santos, M. Weldon, A. Zafar, J. T. Dudman, C. R. Gerfen, A. W. Hantman, W. Korff, S. M. Sternson, N. Spruston, K. Svoboda, and J. Chandrashekar. 2019. 'Reconstruction of 1,000 Projection Neurons Reveals New Cell Types and Organization of Long-Range Connectivity in the Mouse Brain', *Cell*, 179: 268-81 e13.

Wu, D., D. Reisinger, J. D. Xu, S. A. Fatemi, P. C. M. van Zijl, S. Mori, and J. Y. Zhang. 2014. 'Localized diffusion magnetic resonance micro-imaging of the live mouse brain', *Neuroimage*, 91: 12-20.

Wu, D., J. Xu, M. T. McMahon, P. C. van Zijl, S. Mori, F. J. Northington, and J. Zhang. 2013. 'In vivo high-resolution diffusion tensor imaging of the mouse brain', *Neuroimage*, 83: 18-26.

Wu, D., and J. Y. Zhang. 2016. 'In vivo mapping of macroscopic neuronal projections in the mouse hippocampus using high-resolution diffusion MRI', *Neuroimage*, 125: 84-93.

Xu, F., Y. Shen, L. Ding, C. Y. Yang, H. Tan, H. Wang, Q. Zhu, R. Xu, F. Wu, Y. Xiao, C. Xu, Q. Li, P. Su, L. I. Zhang, H. W. Dong, R. Desimone, F. Xu, X. Hu, P. M. Lau, and G. Q. Bi. 2021. 'High-throughput mapping of a whole rhesus monkey brain at micrometer resolution', *Nat Biotechnol*, 39: 1521-28.

Ying, X. 2019. 'An Overview of Overfitting and its Solutions', *2018 International Conference on Computer Information Science and Application Technology*, 1168.

Zingg, B., H. Hintiryan, L. Gou, M. Y. Song, M. Bay, M. S. Bienkowski, N. N. Foster, S. Yamashita, I. Bowman, A. W. Toga, and H. W. Dong. 2014. 'Neural networks of the mouse neocortex', *Cell*, 156: 1096-111.

Zur, R. M., Y. L. Jiang, L. L. Pesce, and K. Drukker. 2009. 'Noise injection for training artificial neural networks: A comparison with weight decay and early stopping', *Medical Physics*, 36: 4810-18.